6-2006

Determination of Uniaxial Residual Stress and Mechanical Properties by Instrumented Indentation

Manhong Zhao
Columbia University

Xi Chen
Columbia University

Jin Yan
University of Delaware

Anette M. Karlsson
Cleveland State University, a.karlsson@csuohio.edu

Publisher's Statement

NOTICE: this is the author's version of a work that was accepted for publication in Acta Materialia. Changes resulting from the publishing process, such as peer review, editing, corrections, structural formatting, and other quality control mechanisms may not be reflected in this document. Changes may have been made to this work since it was submitted for publication. A definitive version was subsequently published in Acta Materialia, 54, 10, (06-01-2006); 10.1016/j.actamat.2006.02.026

Original Citation

Zhao, M., Chen, X., Yan, J., 2006, "Determination of Uniaxial Residual Stress and Mechanical Properties by Instrumented Indentation," Acta Materialia, 54(10) pp. 2823-2832.

Determination of uniaxial residual stress and mechanical properties by instrumented indentation

Manhong Zhao [a], Xi Chen [a,*], Jin Yan [b], Anette M. Karlsson [b]

[a] *Department of Civil Engineering and Engineering Mechanics, Columbia University, 500 West 120th Street, New York, NY 10027-6699, USA*
[b] *Department of Mechanical Engineering, University of Delaware, Newark, DE 19716-3140, USA*

1. Introduction

Instrumented indentation has been shown to be very useful in measuring the elastic and plastic properties of bulk materials and such a technique is well established for stress-free specimens [1–3]. However, residual stresses occur in many structures, usually being induced by the thermal expansion mismatch between different components, or by mechanical and thermal processing. The presence of residual stress has a significant impact on the mechanical reliability of bulk materials and coatings (e.g., fatigue, fracture, corrosion, and wear) [4]. Moreover, the existence of residual stress prior to an indentation experiment strongly affects the indentation load–depth data [5,6]. Therefore, it is very important to understand the correct way of probing the elastic–plastic properties in a stressed specimen, and to deduce the residual stress quickly and effectively from the inverse analysis of an indentation experiment. To the knowledge of authors, in previous theoretical studies (e.g. Refs. [6–10], including our recent effort [5]), the residual stress was taken to be equi-biaxial which permits a simple axisymmetric formulation of the indentation problem.

In a multilayer structure such as a thermal barrier system [11], a ceramic topcoat (the thermal barrier coating) is deposited on top of a metallic bond coat, which is attached to the superalloy substrate. Both topcoat and bond coat are relatively thick, with thickness of the order of 100 μm. The residual stresses in the topcoat and the bond coat are primarily caused by the thermal expansion mismatch with the substrate. For an indentation test normal to the free surface of the topcoat (shown schematically in Fig. 1(a)), the substrate effect is negligible, as long as the indentation depth is small compared to the ceramic coating thickness. In this case, the residual stress in the topcoat can be regarded as equi-biaxial, which can be effectively measured by the techniques proposed earlier [5]. For the thermal barrier coating, the effects of columnar microstructure and porosity during normal indentation have also

* Corresponding author. Tel.: +1 212 854 3787; fax: +1 212 854 6267.
E-mail address: xichen@civil.columbia.edu (X. Chen).

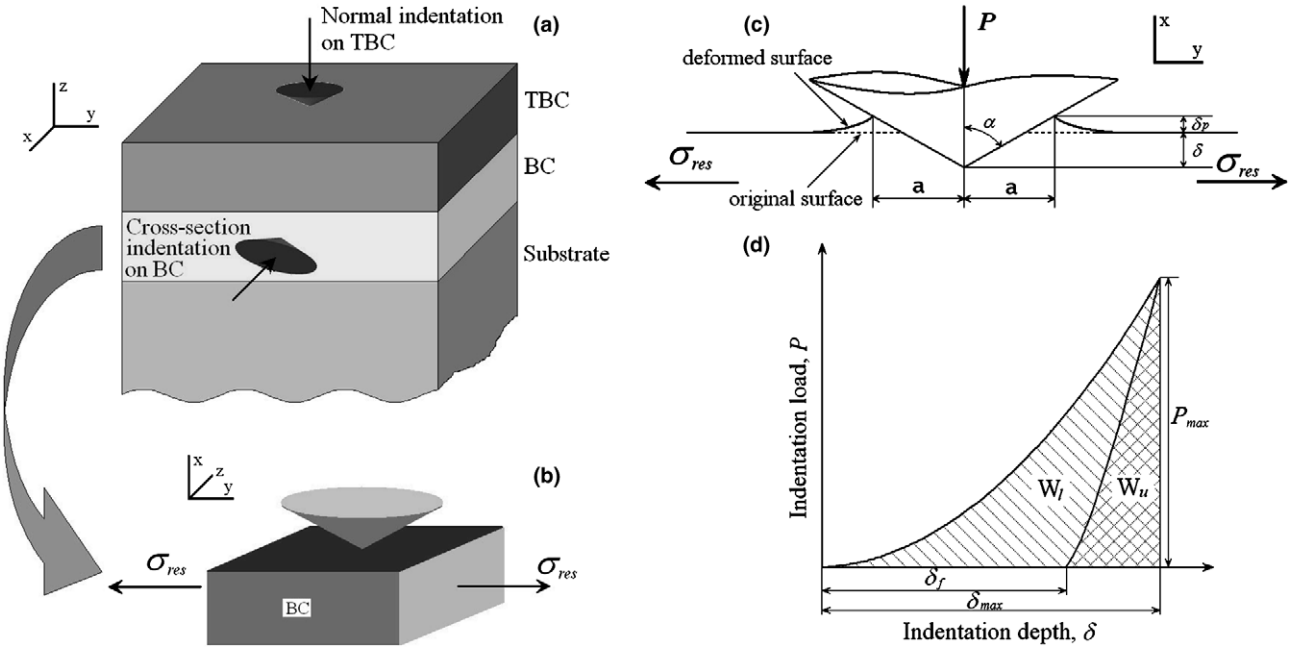

Fig. 1. Schematic of instrumented indentation with a conical indenter. (a) Normal indentation on the topcoat and cross-section indentation on the bond coat of a thermal barrier system. (b) As long as the impression is small, the cross-section indentation may be modeled as an impression on a semi-infinite bulk with uniaxial residual stress. (c) Side view of conical indentation on a specimen with uniaxial in-plane residual stress. (d) Typical indentation depth–load curves obtained from an indentation experiment with loading work and unloading work indicated as the areas enclosed by the curve triangles.

been incorporated in our previous studies [12,13]. However, the mechanical properties and residual stress of all layers in a multilayered system are critical to the system performance; i.e., the bond coat in a thermal barrier system [4,11,14]. Since the bond coat is below the topcoat, the normal indentation technique described above cannot be used to probe directly the intrinsic properties of the bond coat.

One way to access the bond coat is by making a cross-section of the coating and to measure the properties on the cross-section. The specimen is usually sectioned by diamond wire cutting. After mounting, surface grinding, and polishing, the indentation experiment is carried out on the cross-section of the specimen [15] (shown schematically in Fig. 1(a)). If the size of the impression is much smaller than the thickness of the bond coat, the bond coat can be modeled as a semi-infinite and homogeneous bulk material. For an indentation experiment on the cross-section with shallow penetration, the problem can be reduced to normal indentation on a bulk bond coat specimen where the thermal residual stress is essentially uniaxial (Fig. 1(b)). Similarly, the residual stress field induced by mechanical or thermal processing is primarily uniaxial for a range of engineering applications. In all of these cases, the indentation problem becomes three-dimensional. It is therefore important to develop a new indentation technique that effectively measures the mechanical properties and uniaxial residual stress of a bulk specimen from one simple test.

In this paper, a numerical framework is established using three-dimensional finite element analysis, correlating the uniaxial residual stress and the elastic–plastic properties with the indentation load–depth data obtained during loading and unloading. Reverse analysis is used to determine the uniaxial residual stress and mechanical properties of a linear elastic, perfectly plastic specimen. The new technique has been applied to evaluate parallel experiments, where the nanoindentation tests are carried out on the cross-section of a thermal barrier system. The residual stress, elastic modulus, and yield stress of the bond coat are measured and the values are found to agree with those from the literature.

2. Numerical approach

2.1. Model and assumptions

Schematic representations of the three-dimensional model are shown in Figs. 1(b) and (c). The relationship between the indentation force, P, and the indentation depth, δ, during loading and unloading can readily be measured during the experiment and a typical example is given in Fig. 1(d). The friction and the finite compliance of the measuring system and the indenter tip are ignored. We make two simplifications in this study:

(1) The bulk specimen is taken to be linear elastic, perfectly plastic. Such a property is a good approximation for many high-strength alloys and ceramics, including a considerable number of metals, intermetallics, and superalloys, which have small or negligible strain hardening exponents (less than 0.05 or so). Thus, the idealized property applies to the bond coat NiCoCrAl (a multiphase intermetallic) [11,16], which

has motivated this study and been employed in parallel experiments (see below for details). For other materials, the effect of work hardening is also important. This topic is under investigation in our laboratory, the results of which will be published at a later date.

(2) The indenter is taken to be a rigid cone with half-apex angle $\alpha = 70.3°$, with a cross-sectional area equivalent to that of a Berkovich indenter. Even though the indentation problem under investigation is three-dimensional, by using a conical indenter, the alignment issue between the three-sided pyramid Berkovich indenter and the direction of residual stress can be avoided. The indenter tip is taken to be perfectly sharp in the numerical study. Note that the indenter tip used in practice has a finite radius that is typically tens of nanometers, affecting the results for relatively shallow indentations. Such an effect has been neglected in this study.

Young's modulus is denoted by E and the yield stress of the specimen by σ_Y. The Poisson's ratio (v) has been shown to be a minor factor during indentation [17] and it is taken to be 0.3 in this study. The uniaxial residual stress is σ_{res}. If the material is relatively soft (with large E/σ_Y), pile-up will occur around the indenter due to finite plastic deformation and the pile-up height is denoted by δ_p (Fig. 1(c)) [5]. Otherwise, for hard materials with smaller E/σ_Y, material around the indenter will sink in with the tip, producing a negative δ_p [5]. The projected contact radius is given by $a = (\delta + \delta_p)\tan\alpha$. The maximum penetration is δ_{max} and after unloading, the residual penetration is δ_f (Fig. 1(d)). The work done during indentation can be obtained by integrating the loading and unloading curves. The areas under the loading curve and unloading curve are the loading work, $W_l = \int_0^{\delta_{max}} P\,d\delta$, and the unloading work, $W_u = -\int_{\delta_{max}}^{\delta_f} P\,d\delta$ (Fig. 1(d)). In order to obtain sufficiently accurate results and smooth functional forms for both loading and unloading P–δ curves, more than 200 data points are generated from finite element analyses, which are then integrated numerically to obtain the indentation loading work and unloading work.

2.2. Dimensional analysis

Substantial error can occur when measuring the contact radius after unloading due to the large elastic recovery, especially for materials with small E/σ_Y and/or residual compression [5]. As opposed to the classic approach which requires an accurate determination of contact area [1,2], the formulation in this paper uses only the depth–load curve of a conical indentation test. If the strain gradient effect [18] is ignored, dimensional analysis shows that the indentation force P scales with δ^2 if the indenter tip is perfectly sharp [3]. Integration of the indentation load function from zero to the maximum penetration leads to a normalized loading work [19]:

$$\frac{W_l}{\sigma_Y \delta_{max}^3} = \frac{\int_0^{\delta_{max}} P\,d\delta}{\sigma_Y \delta_{max}^3} = f\left(\frac{E}{\sigma_Y}, \frac{\sigma_{res}}{\sigma_Y}\right) \quad (1)$$

where f is a dimensionless function whose form will be determined from numerical analyses, elaborated below. With reference to Fig. 1(d), inspired by the fact that the loading work W_l is normalized by the base of the loading "curve triangle"[1] ($\delta_{max} - 0$), we use the base of the unloading curve triangle ($\delta_{max} - \delta_f$) to normalize the unloading work:

$$\frac{W_u}{\sigma_Y(\delta_{max} - \delta_f)^3} = \frac{-\int_{\delta_{max}}^{\delta_f} P\,d\delta}{\sigma_Y(\delta_{max} - \delta_f)^3} = g\left(\frac{E}{\sigma_Y}, \frac{\sigma_{res}}{\sigma_Y}\right) \quad (2)$$

where g is another dimensionless function, different from f.

Since we have three unknown structural parameters, i.e. the elastic–plastic behavior (E, σ_Y) and the residual stress σ_{res}, we need an additional equation to solve for these unknowns. For a given material, the loading curve triangle is characterized by $P = C\delta^2$ for a sharp indenter [3]. Thus, the curvature C, or, equivalently, the area of the loading work W_l used in this study, is the only variable needed to describe the indentation loading behavior. Furthermore, the unloading curve may be represented by $P = D(\delta - \delta_f)^m$ [3,20] where D and m are two variables depicting the unloading curve triangle. Alternatively, one could use either the unloading work and the contact stiffness (i.e., the slope of the initial portion of the unloading curve) [21,22], or the unloading work and the residual penetration as independent functions. Since the slope of the unloading curve usually is very steep, the measurement of the contact stiffness may result in a large error in both experiment and numerical analyses. By contrast, the indentation depth can be measured with high accuracy in an instrumented indentation experiment. Therefore, in the present study the normalized residual indentation depth, instead of the contact stiffness, is chosen in the dimensionless formulation:

$$\frac{\delta_f}{\delta_{max}} = h\left(\frac{E}{\sigma_Y}, \frac{\sigma_{res}}{\sigma_Y}\right) \quad (3)$$

All three dimensionless equations (Eqs. (1)–(3)),[2] which will be determined by fitting the numerical results obtained from extensive simulations based on the finite element method (FEM), correlate the material properties and the uniaxial residual stress with the indentation force–displacement curves. Finally, by means of these relationships, the material properties (E, σ_Y) as well as uniaxial residual stress σ_{res} can be determined from the reverse analysis.

[1] The term "curve triangle" is used to emphasize that both loading work and unloading work do not make up perfect geometrical triangles.

[2] Note that these three dimensionless functions are valid only when the specimen is semi-infinite. In this case, the indentation depth is the only length quantity involved and the indentation work scales with the cube of indentation depth. If the specimen has finite dimensions, the boundary condition could preclude the use of the dimensional analysis outlined here.

2.3. Finite element analysis

The commercial finite element program ABAQUS [23] was used to simulate the indentation response of a linear elastic, perfectly plastic material with uniaxial residual stress. The three-dimensional mesh is shown in Fig. 2. Based on symmetry, only a quarter of the semi-infinite specimen is modeled, which contains 22,400 eight-node hexahedral elements. The rigid analytical contact surface option was used to simulate the rigid indenter, and the option for finite deformation and strain was employed. Prior to the indentation, a uniform uniaxial residual stress field is introduced into the specimen by means of anisotropic thermal expansion. The material is given a set of anisotropic coefficients of thermal expansion, which result in thermal expansion in only one direction when subjected to a temperature change. Thus, a uniaxial residual stress field can be generated by constraining the expansion in that particular direction. The indentation is displacement controlled by imposing a vertical displacement δ on the rigid indenter, and the reaction force acting on the indenter is multiplied by four to obtain the indentation force P, such that the missing three-quarters of the mesh is accounted for. As already mentioned, more than 200 increments are used during both loading and unloading processes to obtain sufficiently smooth P–δ curves, which are integrated to obtain the loading work and unloading work. The substrate material is taken to be elastic–perfectly plastic, with a Von Mises surface to specify yielding. The Coulomb friction law is used between contact surfaces, and the friction coefficient is taken to be 0.1. We note that friction is a minor factor during indentation [17].

During the forward analysis, the inverse of yield strain E/σ_Y is varied from 10 to 1000, and the residual stress $\sigma_{res}/$

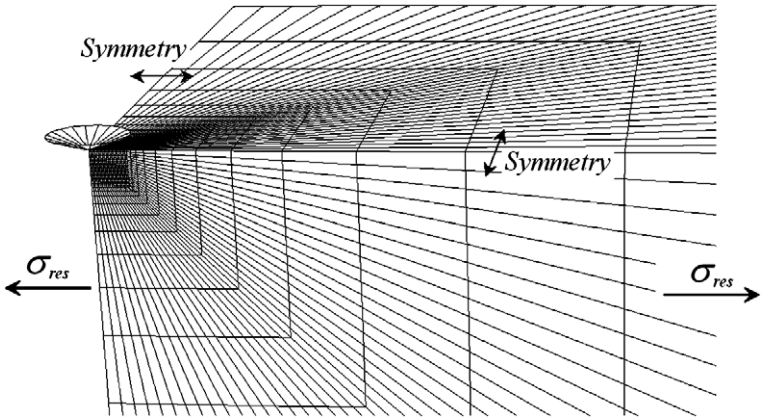

Fig. 2. Three-dimensional finite element mesh used in the analysis.

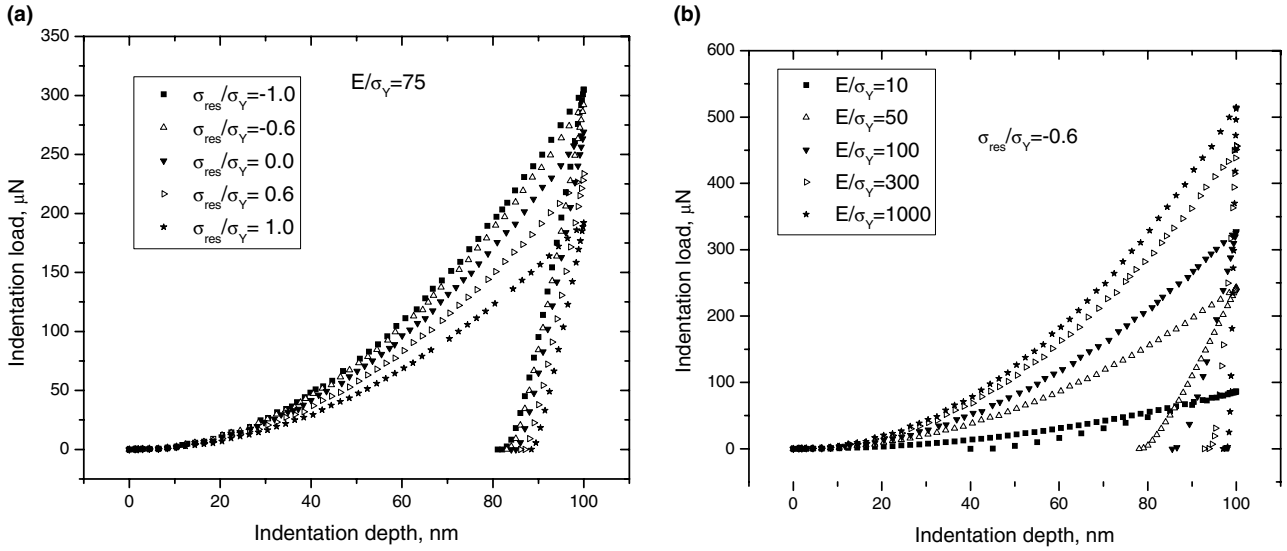

Fig. 3. Indentation depth–load curve obtained from FEM indentation test: (a) σ_{res}/σ_Y varies from -1.0 to 1.0 with $E/\sigma_Y = 75$; (b) E/σ_Y varies from 10 to 1000 with $\sigma_{res}/\sigma_Y = -0.6$.

σ_Y is varied from −1.0 to 1.0. Such a wide range covers almost all possible combinations of mechanical properties and residual stress encountered in engineering materials. For each combination, f, g, and h are computed, as discussed below.

3. Forward analysis

3.1. Force–displacement curves of numerical indentation tests

Selected numerical results of indentation load–depth curves are given in Fig. 3. The effect of residual stress is investigated in Fig. 3(a), where the normalized residual stress σ_{res}/σ_Y varies from −1.0 to 1.0 with E/σ_Y fixed at 75 (with $\sigma_Y = 500$ MPa). In all cases, the force, P, scales with δ^2 during loading. However, the residual compression requires a higher force to indent the material whereas residual tension requires a lower force. The presence of residual stress also affects the unloading curves: the residual indentation depth, δ_f, is smaller for residual compression compared with tension (i.e., the elastic recovery is larger when residual compression is present). The effect of E/σ_Y is given in Fig. 3(b) where σ_{res}/σ_Y equals −0.6, and E/σ_Y varies from 10 to 1000 (with $\sigma_Y = 500$ MPa). When the yield stress and the residual stress are fixed, the larger the Young's modulus, the larger the indentation force needed to achieve the same penetration depth. Since the initial slope of the unloading curve (i.e., contact stiffness) is proportional to the elastic modulus of the material [1], Fig. 3(b) clearly shows the change of the initial unloading with the variation of Young's modulus. Moreover, as E/σ_Y increases (i.e., the material becomes more plastic), the residual indentation depth gets larger due to smaller elastic recovery.

3.2. Dimensionless functions

The three dimensionless functional forms of Eqs. (1)–(3) with regard to the normalized loading work, unloading work, and residual indentation depth are obtained by fitting the FEM indentation results within the range of material properties considered in this paper (e.g. the P–δ curves in Fig. 3):

Table 1
The coefficients of the three dimensionless equations (4)–(6)

Coefficients a_i, b_i, or c_i	Normalized work of indentation	Normalized unload work	Normalized residual indentation depth
1	15.213164	−31.856348	−0.418401
2	2.745044	32.787868	0.576243
3	−2.344048	−11.618976	−0.084057
4	−0.035888	1.99308	0.004318
5	−1.907872	−0.11564	0.211673
6	−13.002132	20.66082	−0.059685
7	−0.353668	−20.653648	0.004239
8	2.663928	7.266008	0.695656
9	−0.690204	−0.946536	−0.537857
10	4.648624	0.039888	0.156193
11	−0.538512	−100.609152	−0.019944
12	−0.71608	137.622188	9.407218×10^{-4}
13	0.169124	−71.122976	0.254452
14	−0.347016	17.448792	−0.170792
15	0.073968	−2.032584	0.042547
16	0.057928	0.0905	−0.004655
17	−0.011368	−83.468468	1.888338×10^{-4}
18		110.87762	
19		−55.7215	
20		13.31378	
21		−1.518592	
22		0.066588	

where $\xi = \ln(E/\sigma_Y)$ and $\eta = \sigma_{res}/\sigma_Y$. The coefficients a_i, b_i, and c_i are tabulated in Table 1. Fig. 4 shows these three dimensionless functional forms as three-dimensional continuous surfaces, and the data obtained from FEM simulations are shown by black dots. The agreement between the original data points and fitted functions is quite good, with errors of less than 2%. Note that we have adopted the normalized unloading work and residual penetration as dimensionless variables in this study, which leads to smoother fitting functions and smaller errors compared with previous studies [5,21]. The smooth functions also help to converge the reverse analysis.

4. Reverse analysis

4.1. Principle of the reverse analysis

Three unknown structural parameters must be determined, i.e. the elastic–plastic behavior (E/σ_Y) and the

$$\frac{W_l}{\sigma_Y \delta_{max}^3} = f\left(\frac{E}{\sigma_Y}, \frac{\sigma_{res}}{\sigma_Y}\right) \equiv F(\xi,\eta) = a_1 + a_2\eta + a_3\eta^2 + a_4\eta^3 + a_5\eta^4 + (a_6 + a_7\eta + a_8\eta^2 + a_9\eta^3)\xi + (a_{10} + a_{11}\eta + a_{12}\eta^2 + a_{13}\eta^3)\xi^2 + (a_{14} + a_{15}\eta + a_{16}\eta^2 + a_{17}\eta^3)\xi^3 \quad (4)$$

$$\frac{W_u}{\sigma_Y(\delta_{max} - \delta_f)^3} = g\left(\frac{E}{\sigma_Y}, \frac{\sigma_{res}}{\sigma_Y}\right) \equiv G(\xi,\eta) = b_1 + b_2\xi + b_3\xi^2 + b_4\xi^3 + b_5\xi^4 + (b_6 + b_7\xi + b_8\xi^2 + b_9\xi^3 + b_{10}\xi^4)\eta + (b_{11} + b_{12}\xi + b_{13}\xi^2 + b_{14}\xi^3 + b_{15}\xi^4 + b_{16}\xi^5)\eta^2 + (b_{17} + b_{18}\xi + b_{19}\xi^2 + b_{20}\xi^3 + b_{21}\xi^4 + b_{22}\xi^5)\eta^3 \quad (5)$$

$$\frac{\delta_f}{\delta_{max}} = h\left(\frac{E}{\sigma_Y}, \frac{\sigma_{res}}{\sigma_Y}\right) \equiv H(\xi,\eta) = c_1 + c_2\xi + c_3\xi^2 + c_4\xi^3 + (c_5 + c_6\xi + c_7\xi^2)\eta + (c_8 + c_9\xi + c_{10}\xi^2 + c_{11}\xi^3 + c_{12}\xi^4)\eta^2 + (c_{13} + c_{14}\xi + c_{15}\xi^2 + c_{16}\xi^3 + c_{17}\xi^4)\eta^3 \quad (6)$$

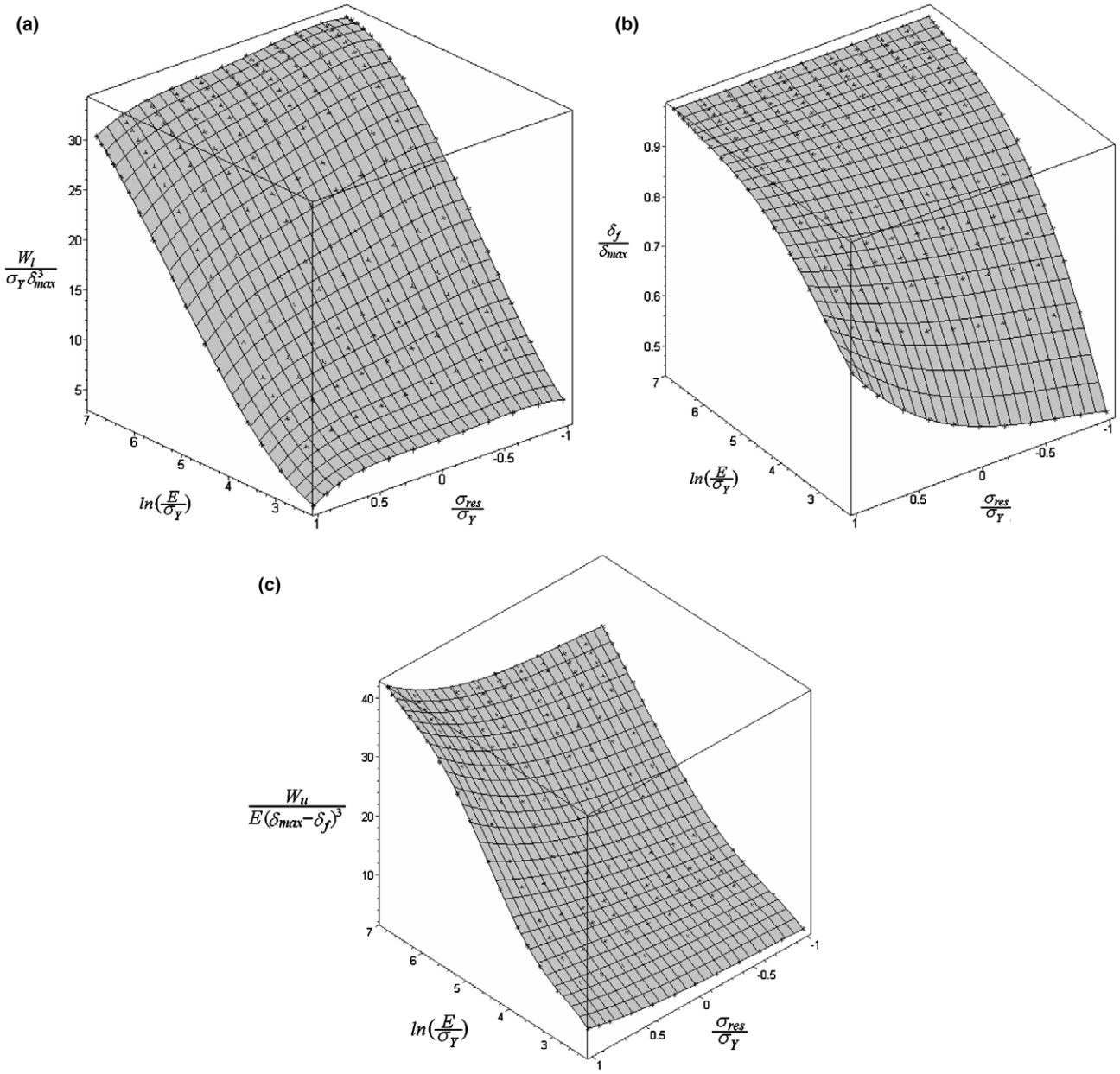

Fig. 4. Fitting surfaces of the three dimensionless equations (4)–(6), where the black dots represent the indentation data obtained from FEM simulations.

residual stress σ_{res}. A flow chart of the reverse analysis algorithm is given in Fig. 5. From an instrumented indentation test, the loading work, unloading work, maximum indentation depth, and residual indentation depth can easily be determined. Within a wide range of E, σ_Y, and σ_{res}, for each possible combination of elastic–plastic behavior and residual stress, the errors of the three dimensionless equations with respect to the measurement are calculated. The total error is defined as the summation of the absolute values of the three errors, and the combination of material properties leading to the smallest total error is selected as the solution.

4.2. Numerical examples of the reverse analysis

The material responses from the numerical indentation tests are used to check the effectiveness of the reverse analysis algorithm. FEM indentation experiments are carried out with different material combinations (E/σ_Y, σ_{res}/σ_Y).[3] The resulting load–depth data are employed to calculate indentation parameters (i.e., W_l, W_u, δ_{max}, δ_f), from which the material properties and residual stress $(E/\sigma_Y, \sigma_{res}/\sigma_Y)|_{reverse}$ are

[3] Some of these parametric combinations are not used in the forward analysis in determining the functional forms of Eqs. (4)–(6).

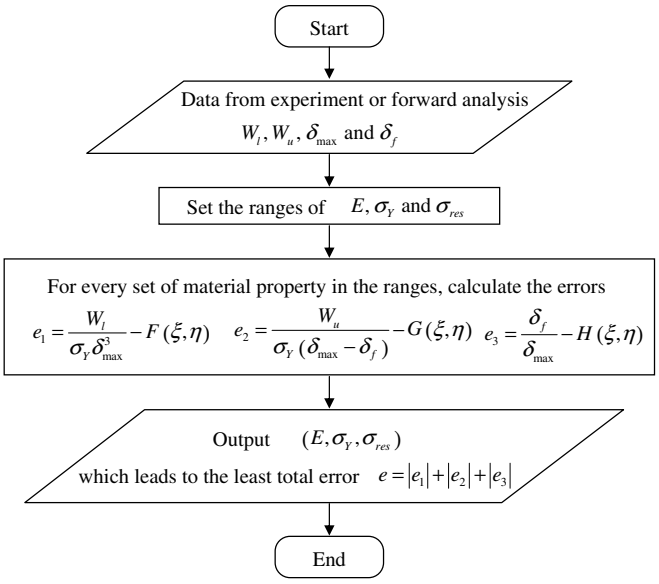

Fig. 5. The flow chart for determining material properties and uniaxial residual stress using the reverse analysis.

obtained from the reverse analysis. The comparisons between the material combinations identified from the reverse analysis and the input material combinations used in the numerical experiments are shown in Fig. 6, where E/σ_Y is varied between 10 and 1000 and σ_{res}/σ_Y is varied from -1.0 to 1.0. The end of each arrow is the input parameter $(E/\sigma_Y, \sigma_{res}/\sigma_Y)$ for the numerical experiment, whereas the tip of each arrow is the result determined from the reverse analysis $(E/\sigma_Y, \sigma_{res}/\sigma_Y)|_{reverse}$. The length of the arrow indicates the total error. Most calculated combinations match the input combinations very well with an error smaller than 10%. Compared with the error of E/σ_Y, the error of σ_{res}/σ_Y is larger, especially for large residual tension. This is partly because the fitting functions (Eqs. (4)–(6)) are only valid within the data range used in this paper, i.e. $E/\sigma_Y = 10$–1000 and $\sigma_{res}/\sigma_Y = -1.0$ to 1.0. When the material property combination is near the limit of such a range, the numerical results of the reverse analysis may approach the correct solution from only one direction, which tends to produce a larger error.

4.3. Error sensitivity analysis of the numerical study and discussion

In any given example of the reverse analysis shown in Fig. 6, the indentation parameters (W_1, W_u, δ_{max}, δ_f) are obtained from a numerical experiment and they do not fall exactly on the three-dimensional surfaces of fitting equations (4)–(6) (cf. Fig. 4). This is the source of numerical error between input material parameter (end of arrow) and identified material property from the reverse analysis (tip of arrow). If the indentation parameters (W_1, W_u, δ_{max}, δ_f) fall exactly on the three-dimensional surfaces, the error of the reverse analysis vanishes.

During an instrumented indentation experiment, the indentation depth δ_{max} and the residual penetration δ_f may be measured accurately from the P–δ curve. However, due to experimental "noise", small errors may accumulate in W_1 and W_u via integration of the P–δ data. Thus, we will here conduct an error sensitivity analysis. First, W_1 is given

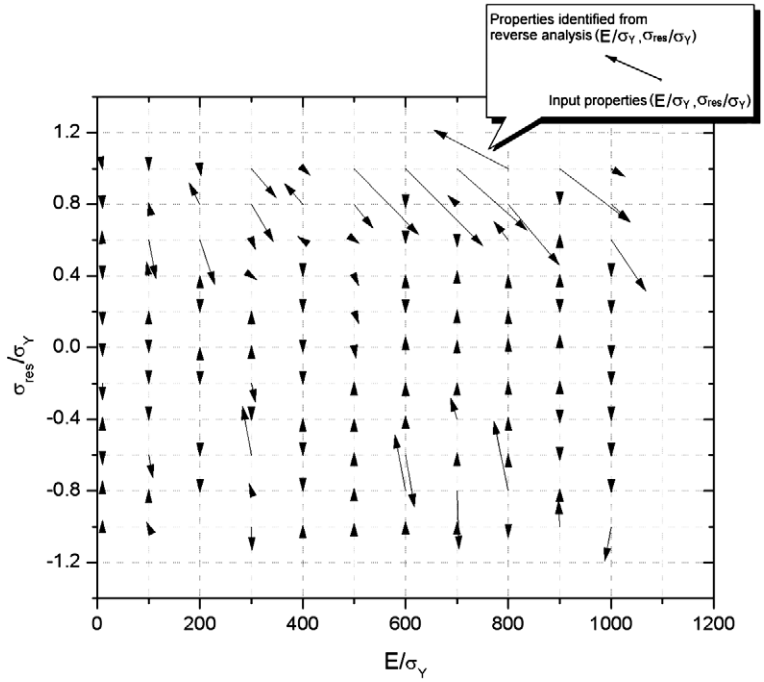

Fig. 6. Comparison between the input material combinations used in FEM indentation experiments (end of arrow) and the material combinations identified from the reverse analysis (tip of arrow).

a 2% error while the other three parameters (W_u, δ_{max}, δ_f) are located exactly on the three-dimensional surfaces (Eqs. (4)–(6)). From the new set of parameters ($W_l|_{error}$, $W_u|_{exact}$, $\delta_{max}|_{exact}$, $\delta_f|_{exact}$), reverse analyses are carried out to identify material properties (tip of arrow), which are compared with the input parameters (end of arrow) in Fig. 7(a). In most cases, the resulting error is relatively small and the error of E obtained from the reverse analysis ranges from −5% to 8%, the error of σ_Y is between −20% and 23%, and the error of σ_{res} is from −31% to 37%. Note that the magnitude of the error of E and σ_Y is comparable with the reverse analyses employed in other indentation problems (e.g. Ref. [24]), and the residual stress is more sensitive to the error in experimental data.

A similar analysis is carried out by introducing 2% error to the unloading work. The reverse analysis results based on ($W_l|_{exact}$, $W_u|_{error}$, $\delta_{max}|_{exact}$, $\delta_f|_{exact}$) are shown as the arrow tips in Fig. 7(b) and compared with input parameters

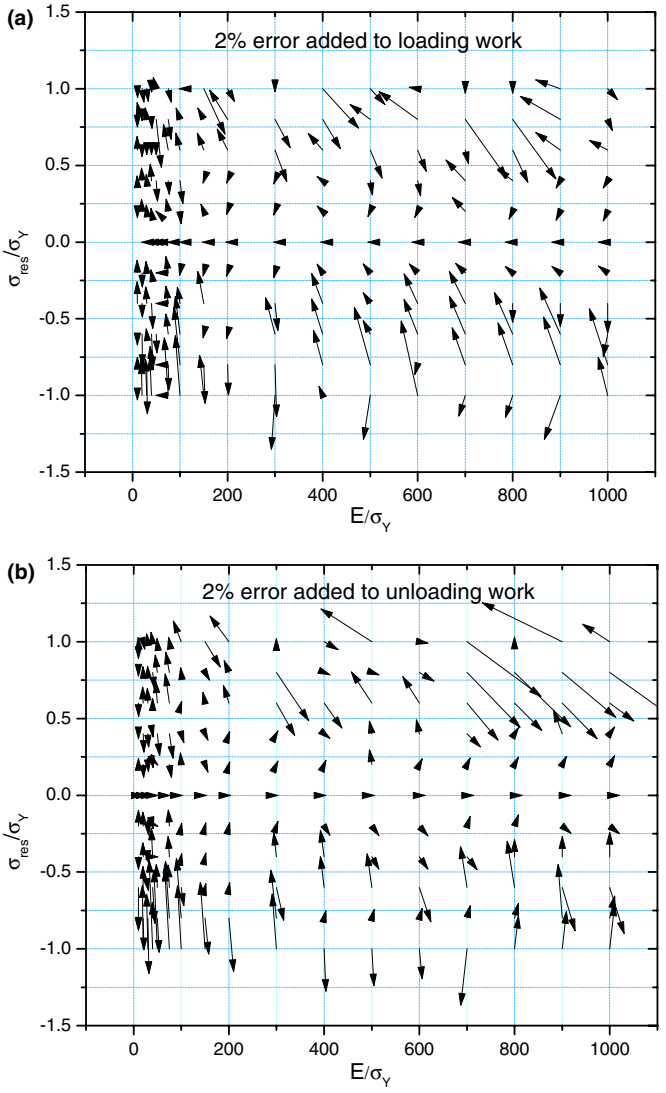

Fig. 7. Error sensitivity analysis (a) with 2% error in loading work; (b) with 2% error in unloading work: the reverse analysis is compared with input parameter.

(end of arrow). In this case, the error of E obtained from the reverse analysis ranges from −4% to 10%, the error of σ_Y is between −16% and 27%, and the error of σ_{res} is from −26% to 42%. Note that these values represent the extreme cases of error; in most cases, the error is significantly smaller.

The error sensitivity analysis discussed above corresponds to the idealized numerical problem, that is, a numerical experiment of a sharp conical indentation on a semi-infinite linear elastic, perfectly plastic specimen. In real experiments, the finite indenter tip radius, finite size of the specimen, and non-negligible strain hardening of some materials will impose considerable errors on the method introduced in this paper. Therefore, the practical application of the present study is limited to indentation experiments with a moderate impression size, which should be small compared with the specimen dimension but large compared with the indenter tip radius. Moreover, the material is required to have small or negligible strain hardening behavior. In the absence of residual stress, the effect of strain hardening and proper ways of measuring the work hardening exponent by conical indentation have been proposed [21,25]. The combined effect of residual stress and work hardening on the indentation characteristics exceeds the scope of this paper; it is under investigation and will be published elsewhere.

4.4. Application to indentation experiment on a thermal barrier system

We will now attempt to use the proposed technique to extract the elastic–plastic properties and the residual stress of a bond coat, based on a nanoindentation experiment of the cross-section as shown schematically in Figs. 1(a) and (b). The particular bond coat investigated has the composition $Ni_{38}Co_{19}Cr_{21}Al_{22}$. It provides oxidation protection for the superalloy substrate (cf. Fig. 1(a)) by providing aluminum to the aluminum oxide scale forming between the bond coat and topcoat. The topcoat, the thermal barrier coating itself, is deposited by the electron beam physical vapor deposition technique. The specimen is thermally cycled between 200 and 950 °C for 300 h in 10 min cycles [26]. In combination with high-temperature yielding and creep, and thermal expansion mismatch, residual stress develops in the bond coat at ambient temperature. The rapid cooling (forced air) indicates that negligible stress relaxation occurs during cooling. The cross-section of the thermal barrier system is made by diamond wire cutting, followed by mounting, hand grinding, diamond spray grinding, and polishing. To obtain quality scanning electron microscopy (SEM) images, ion etching and gold coating are carried out. Fig. 8(a) shows the SEM image of the cross-section of the bond coat where nine impressions were made using a Berkovich indenter. These impressions are spaced apart to avoid interference. The impression size (about 2 μm in diameter) is much smaller than the bond coat thickness (100 μm) yet much larger than the typical indenter tip radius (~60 nm). Moreover, the strain hardening of the bond coat may be neglected, it being an intermetallic

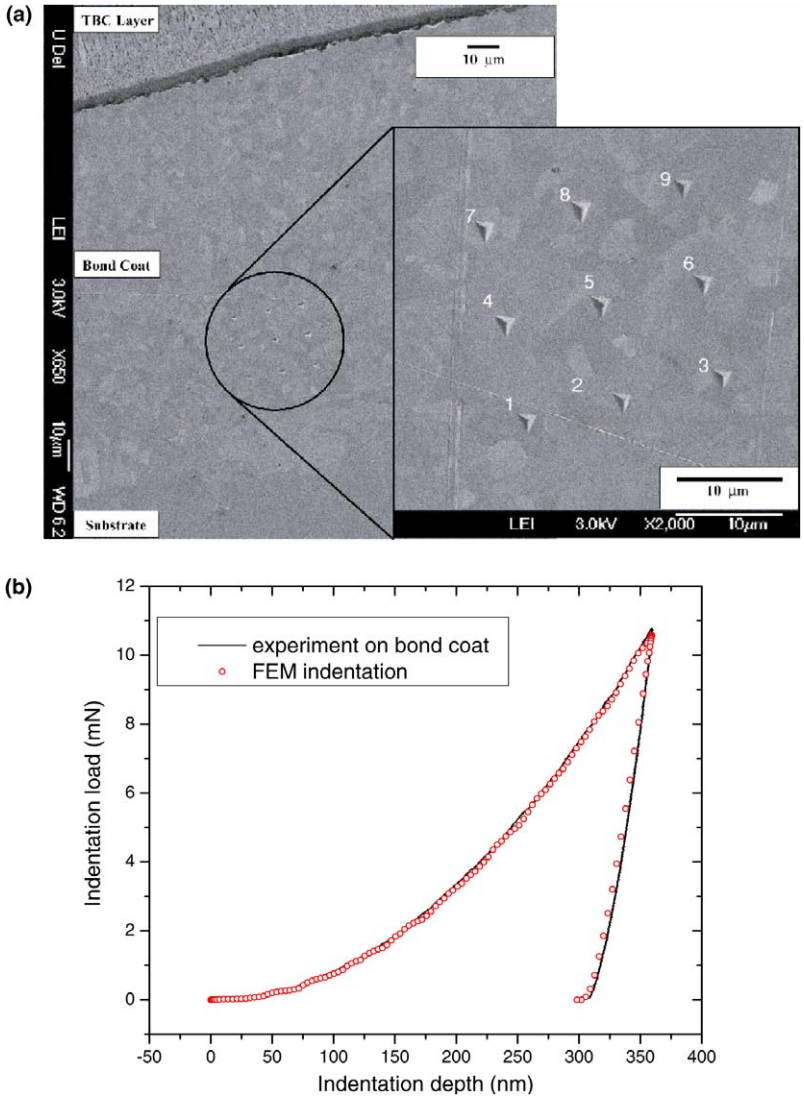

Fig. 8. (a) SEM image of indentation impressions on the cross-section of bond coat. (b) The indentation load–depth curve of the sixth impression (solid line), which agrees well with the numerical indentation load–depth curve using the material properties identified from the reverse analysis.

compound [11,16]. Thus, all three basic assumptions are satisfied and the use of the current model is justified.

Fig. 8(b) shows the experimental indentation force–displacement curve (solid line) measured from the sixth impression in Fig. 8(a).[4] From this representative experimental curve, the indentation parameters are determined as $W_l = 1.29$ N nm, $W_u = 0.241$ N nm, $\delta_{max} = 359.3$ nm, and $\delta_f = 301.9$ nm. By substituting these values into the reverse analysis, the material properties and uniaxial residual stress can be determined: $E = 112$ GPa, $\sigma_Y = 1.34$ GPa, and $\sigma_{res} = -0.95$ GPa. These material properties are then used as input parameters to a numerical indentation test, and the resulting indentation load–depth curve (dotted curve) is calculated and compared to the experimental curve in Fig. 8(b) – the good agreement verifies the measured elastic–plastic properties and residual stress. Finally, by analyzing all nine impressions, the average Young's modulus of the bond coat is about $E = 115$ GPa, yield stress $\sigma_Y = 1.3$ GPa, and residual compression is about $\sigma_{res} = -0.91$ GPa. These values are close to what has been typically measured for bond coats [11,16]; however, the exact values are not available. Suppose the residual stress is caused by the thermal expansion mismatch: a first-order estimation of the residual stress in the bond coat is given by $E\Delta\alpha\Delta T/(1-\nu)$, where $\Delta T \approx 950\,^{\circ}\mathrm{C}$, and $\Delta\alpha$ of about $-4\times10^{-6}/^{\circ}\mathrm{C}$ is the difference between the thermal expansion coefficient of the bond coat and the substrate [16]. This leads to a residual stress of about -0.62 GPa, which qualitatively agrees with the indentation measurement.

Other than the errors caused by the small deviations from the three basic assumptions discussed above, there are several factors contributing to the difference between

[4] The experiment is force controlled. Due to an initial error possibly due to calibration, the P–δ shown here has been shifted to the right for about 80 nm compared with the original data. Such a shift is based on the assumption that P should scale with δ^2 during loading when the tip radius effect is ignored.

the uniaxial residual stress measured by our proposed indentation model and that estimated from thermal expansion mismatch. Firstly, there is a range of uncertainty of the thermal expansion coefficients and Young's modulus of the individual layers [4,16]. Secondly, the cyclic loading may redistribute the residual stress. Thirdly, the bond coat specimen surface has been polished prior to indentation, which may introduce additional residual stresses. Fourthly, the impression is comparable with the grain size of the bond coat, and the effect of microstructure (e.g., grain boundary and different residual stress in different grains) is not taken into account in our model. Lastly, the indenter used in the experiment is a Berkovich indenter whereas a conical indenter is used in the model, which may have caused errors. Indeed, the comparison between theory and experiment discussed above should be regarded as a qualitative order-of-magnitude estimation. Further experimental studies are needed to validate and improve the indentation technique proposed in this paper.

5. Conclusion

A new indentation technique which effectively measures the uniaxial residual stress and material properties of an elastic–perfectly plastic specimen is proposed. The numerical framework is established under the following premises: (a) the inner layer (or specimen) is relatively thick (or large) compare with the impression size; (b) the indentation depth is large compared with the tip radius; and (c) the material is essentially elastic–perfectly plastic. The normalized loading work, unloading work, and residual indentation depth are computed from extensive three-dimensional FEM indentation simulations, and fitted by smooth dimensionless functions. The effectiveness of the reverse analysis method is verified by the good agreement between the input parameters used for numerical forward analysis and the results identified from the numerical reverse analysis. The reverse analysis algorithm is also used to guide the indentation experiment and to extract the material properties and uniaxial residual stress in the bond coat of a thermal barrier system. When the aforementioned assumptions are satisfied, the results in this paper are useful for measuring the mechanical properties and residual stresses of an inner layer in a multilayer system, as well as in other situations involving uniaxial residual stress. Future experimental work is needed to further validate the residual stress measurement, and numerical studies will be extended to understand the effect of strain hardening.

Acknowledgments

The work of M.Z. and X.C. is supported by NSF CMS-0407743. The work of J.Y. and A.M.K. is supported by NSF DMR-0346664 and ONR N00014-04-1-0498. We thank Professor Christopher Schuh's group at the Massachusetts Institute of Technology for aiding in the nanoindentation tests and Dr. Ing. Marion Bartsch's group at the German Aerospace Center (DLR), Cologne, Germany, for providing the samples.

References

[1] Oliver WC, Pharr GM. J Mater Res 1992;7:1564–83.
[2] Pharr GM. Mater Sci Eng A 1998;253:151–9.
[3] Cheng YT, Cheng CM. Mater Sci Eng R 2004;44:91–149.
[4] Shi J, Darzens S, Karlsson AM. Mater Sci Eng A 2005;392:301–12.
[5] Chen X, Yan J, Karlsson AM. Mater Sci Eng A 2006;416:139–49.
[6] Xu Z, Li X. Acta Mater 2005;53:1913–9.
[7] Suresh S, Giannakopoulos AE. Acta Mater 1998;46:5755–67.
[8] Carlsson S, Larsson PL. Acta Mater 2001;49:2179–91.
[9] Carlsson S, Larsson PL. Acta Mater 2001;49:2193–203.
[10] Swadener JG, Taljat B, Pharr GM. J Mater Res 2001;16:2091–102.
[11] Evans AG, Mumm DR, Hutchinson JW, Meier GH, Petit FS. Prog Mater Sci 2001;46:505–53.
[12] Chen X, Hutchinson JW, Evans AG. Acta Mater 2004;52:565–71.
[13] Chen X, Xiang Y, Vlassak JJ. J Mater Res 2006;21:715–24.
[14] Freund LB, Suresh S. Thin film materials: stress, defect formation and surface evolution. Cambridge: University Press; 2003.
[15] Kim CH, Heuer A. J Mater Res 2004;19:351–6.
[16] Karlsson AM, Hutchinson JW, Evans AG. J Mech Phys Solids 2002;50:1565–89.
[17] Mesarovic SD, Fleck NA. Proc Roy Soc Lond A 1999;455:2707–28.
[18] Fleck NA, Hutchinson JW. Adv Appl Mech 1997;33:295–361.
[19] Yan J, Chen X, Karlsson AM. J Eng Mater Tech [in press].
[20] Pharr GM, Bolshakov A. J Mater Res 2002;17:2660–71.
[21] Ogasawara N, Chiba N, Chen X. Scripta Mater 2006;54:65–70.
[22] Zhao M, Ogasawara N, Chiba N, Chen X. Acta Mater 2006;54:23–32.
[23] ABAQUS. ABAQUS 6.4 user's manual. ABAQUS Inc.; 2004.
[24] Dao M, Chollacoop N, VanVliet KJ, Venkatesh TA, Suresh S. Acta Mater 2001;49:3899–918.
[25] Ogasawara N, Chiba N, Chen X. J Mater Res 2005;20:2225–34.
[26] Bartsch M, Marci G, Mull K, Sick C. Adv Eng Mater 1999;2:127–9.